Supplementary Information: Epitaxial Growth of 2D Manganese Dibromide Thin films on Au(111) with Buffering Overlayers

Zhanze Wang,[1,2] Mingyue Sun,[1,2] Yuedong Wang,[3] Zhipeng Jiao,[1,2] Cong Hong,[1] Qixing Wang,[4] Yujie Zheng,[5,] * Yu Li Huang[1,] *

[1]Joint School of National University of Singapore and Tianjin University, The International Joint Institute of Tianjin University, Fuzhou, Tianjin University, Tianjin 300072, P. R. China

[2]Department of Physics, National University of Singapore, Singapore,117542, Singapore

[3]School of Physics, Hunan Key Laboratory of Super-microstructure and Ultrafast Process, Central South University, 932 South Lushan Road, Changsha, Hunan 410083, P. R. China

[4]Department of Physics, College of Physical Science and Technology, Xiamen University, Xiamen 361005, China

[5]National Innovation Center for Industry-Education Integration of Energy Storage Technology, MOE Key Laboratory of Low-grade Energy Utilization Technologies and Systems, CQU-NUS Renewable Energy Materials & Devices Joint Laboratory, School of Energy and Power Engineering, Chongqing University, Chongqing 400044, China

* Email: zhengyujie@cqu.edu.cn

* Email: hyl@fztju.org.cn

Contents:

I. Calculated lattice constants and bandgaps

We employed both the PBE and HSE06 functions for the calculations. The PBE method has been widely used for preliminary analysis due to its high computational efficiency, but encounters a severe bandgap underestimation for semiconductors and insulators.[1] In comparison, the HSE06 hybrid functional incorporates a short-range Hartree–Fock exchange term under screened Coulomb potential, effectively mitigating self-interaction errors.[2] This correction enhances the accuracy of the calculated band edges, generally yielding bandgap values in closer agreement with experimental observations.

The calculated lattice constants and bandgap values of $MnBr_2$ are summarized in Table S1. The results show a good agreement with previously reported experimental and theoretical data,[3] confirming the reliability of the employed computational approaches. The in-plane lattice parameter *a* remains nearly constant (3.84~3.85 Å) for all the layer numbers, and the out-of-plane lattice parameter *c* decreases slightly from 6.46 Å (monolayer) to 6.24 Å (bulk). Specifically, the PBE-calculated bandgap is 1.2 eV, while the HSE06 functional yields a value of 3.7 eV. Notably, the bandgap almost remains constant from monolayer to trilayer and bulk, highlighting the layer-independent electronic behavior of $MnBr_2$.

Table S1. Summary of the calculated lattice parameters and bandgaps of monolayer, bilayer, trilayer, and bulk $MnBr_2$.

	Monolayer	**Bilayer**	**Trilayer**	**Bulk**
***a* (Å)**	**3.85**	**3.84**	**3.85**	**3.85**
***c* (Å)**	**--**	**6.46**	**6.25**	**6.24**
Bandgap (PBE) (eV)	**1.2**	**1.2**	**1.2**	**1.2**
Bandgap (HSE06) (eV)	**3.7**	**3.7**	**3.7**	**3.6**

II. Optimizing the growth conditions

Figure S1a and S1b show the topographic images of clean Au(111) surface with typical herringbone structures. In Figure S1a, the [$\bar{1}10$] crystallographic direction of Au(111) substrate is indicated by a green arrow, while the [$\bar{1}\bar{1}2$] direction is marked with a yellow arrow. The atomically resolved STM image is demonstrated in Figure S1c, where the unit cell of Au(111) is highlighted by a red parallelogram with a lattice constant of 2.9 Å ± 0.1 Å. The STS spectra in Figure S1d show clear surface states of Au(111) locating at -500 mV to -470 mV, with slight intensity difference between the hcp and fcc regions. In the clean Au(111), the total width (W) of the fcc and hcp regions is 6.6 nm ± 0.06 nm, consistent with the reported 23×√3 reconstructed structure.[4, 5] We also measured the length (L) of the herringbones, which are typically in the range of 5.3 nm to 40.1 nm (Table S2). In fact, the formation of the herringbone structure is very sensitive to the Au(111) steps and surface adsorbates, including contaminations, adatoms, and adlayers, as shown in Figure S1e and S1f.

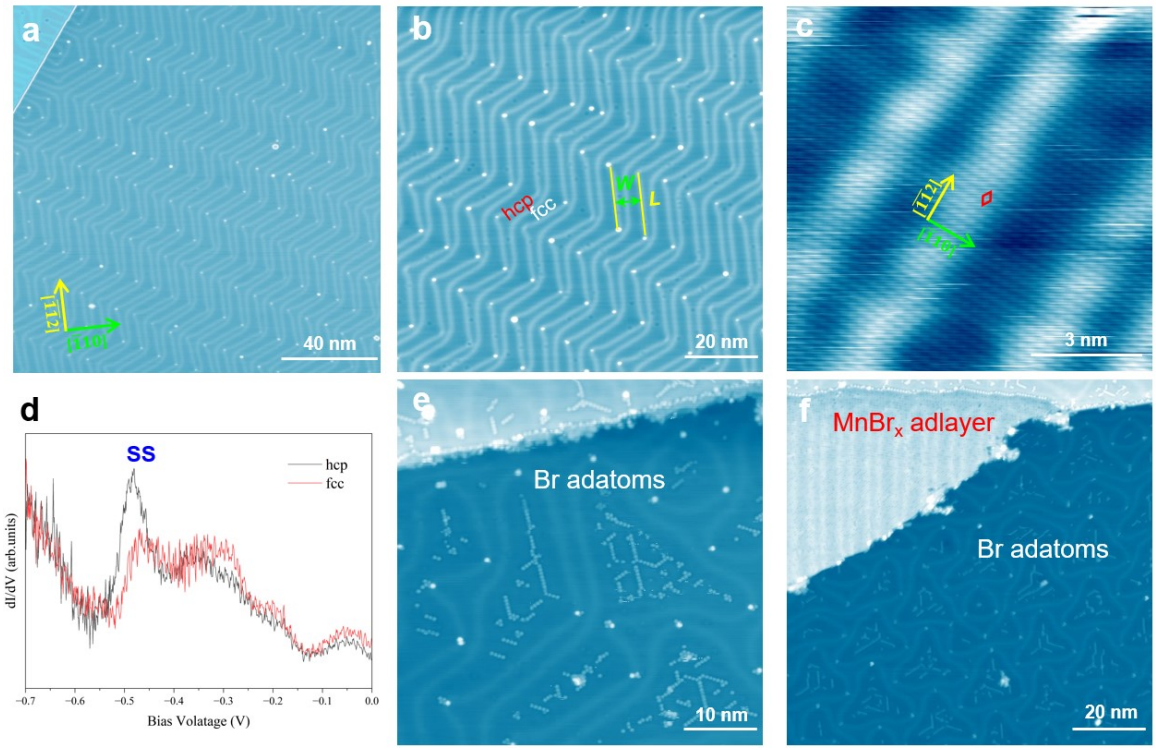

Figure S1. STM images of Au(111). (a) A large-scale STM image of the Au(111) herringbone structure. (b) Zoom-in image (100×100 nm^2) of (a). (c) Atomically resolved image of Au(111) (10×10 nm^2). (d) dI/dV spectra of Au(111). The black line and the red line represent the STS spectra recorded at the hcp and fcc regions, respectively. (e) The formation of irregular herringbones with the adsorption of Br atoms (50×50 nm^2). (f) The reconstructed structure of Au(111) surface is modified by the MnBr$_x$ adlayer (100×100 nm^2). (a-b) V = 1 V, I = 100 pA; (c) V = 10 mV, I = 8.3 nA; (e) V = 0.2 V, I = 400 pA; (f) V = 1 V, I = 400 pA.

MnBr$_2$ (Thermo Scientific, purity over 99.9%) was evaporated from Knudsen cells at 270℃-320℃ with deposition rates of 0.01-0.03 ML per minute. Initially, we hold the Au(111) substrate at room temperature and deposited the MnBr$_2$ source (270℃) onto the surface for 10 minutes. As shown in Figure S2a, the Au(111) surface is almost fully covered with amorphous MnBr$_x$ thin film (>1 ML), where clusters are aggregated together without ordered crystalline structure. Subsequently, the sample was annealed at 100℃ for 30 minutes. Some triangular islands were observed on the top layer as shown in Figure S2b, but the surface is still not uniform. By increasing the annealing temperature to 150℃, the sample surface becomes flattened, and some

nano-stripes appear coexisting with small nanoclusters (Figure S2c). These observations indicate that annealing at elevated temperatures could facilitate the growth of 2D $MnBr_x$ crystals.

In the following, the Au(111) substrate was hold at 100°C during the deposition. After evaporating the $MnBr_2$ source at 290°C for 30 minutes, the overall coverage was only ~0.3 ML. From the large-scale STM image shown in Figure S2d, it can be seen that atomically flat islands form on the surface together with small nanoclusters. Again, the sample was subsequently annealing at 150°C and 185°C for 30 minutes, as shown in Figure S2e and S2f, respectively. Obviously, small clusters disappear after annealing, and large $MnBr_x$ islands form with atomically smooth surface. Herringbone-like patterns are also visible, which extend over hundred nanometers in Figure S2f. As discussed in below and the main text, these are $MnBr_x$ buffering layers (x<2) but not $MnBr_2$ layers.

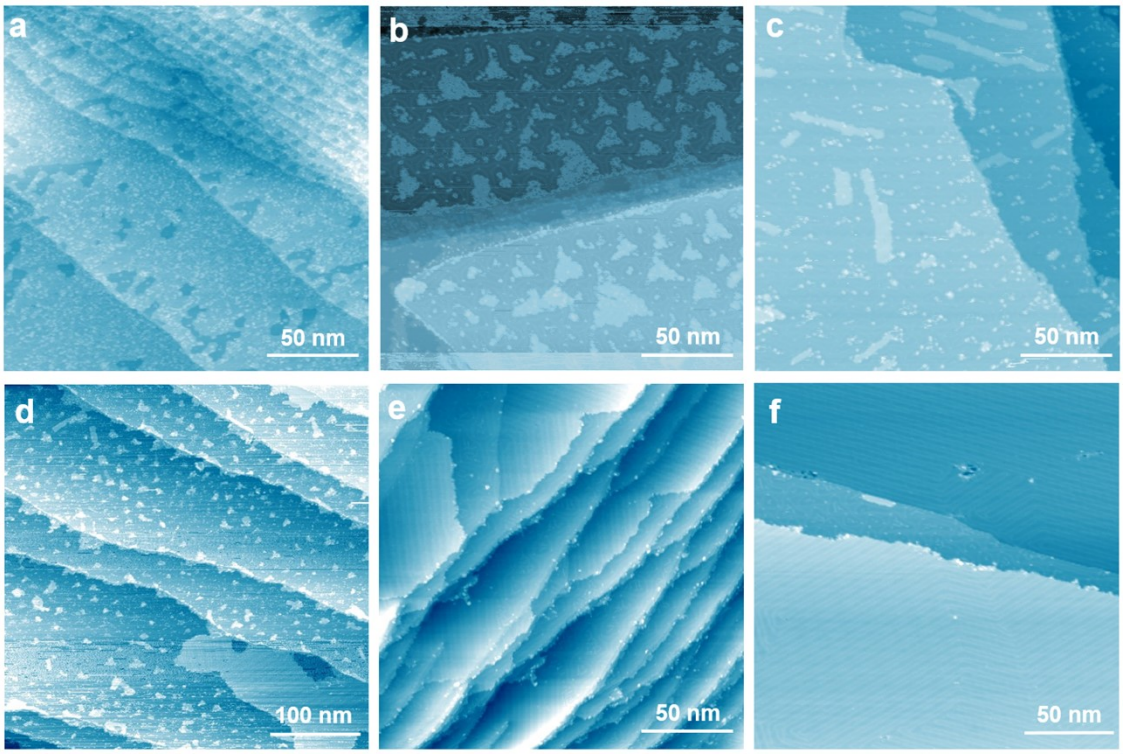

Figure S2. Depositing $MnBr_2$ source onto Au(111) under different conditions. (a) Amorphous $MnBr_x$ thin film (>1 ML) was formed when the substrate was kept at room temperature. (b) After annealing the sample (a) at

100°C for 30 minutes, amorphous triangular islands were observed. (c) The sample was further annealed at 150°C for 30 minutes, where the surface became flattened. (d) Atomically flat $MnBr_x$ islands were grown when the substrate was kept at 100°C during the deposition. (e) The sample was subsequently annealed at 150°C for 30 minutes. (f) The sample was further annealed at 185°C for 30 minutes. (a-b) V = 1 V, I = 60 pA; (c) V = 1 V, I = 140 pA; (d,f) V = 1 V, I_t = 100 pA; (e) V = 1 V, I = 200 pA.

III. Buffering layers

Other buffering layers with less ordering or more defects are also observable as shown in Figure S3. From the large-scale images, e.g., Figure S3a and S3e, it is difficult to distinguish the different phases from each other. Zoom in on the yellow square in Figure S3a, Figure S3b shows that BuffL-I at the lower left corner is easy to be identified with loose-packing atomic structure. In the right side, it gradually transfers to a transitional phase with higher atom density of ~6.1 atom/nm^2. Figure S3c-f demonstrate other close-packing configurations with vacancies and defects. More interesting, we find that the width of the herringbone structure observed in Figure S3f increases to ~7.2 nm, and the length can reach over 100 nm, indicating a new reconstruction of the underneath Au(111) surface. Such interfacial reconstruction might be induced by the interfacial strain between the $MnBr_x$ adlayerand Au(111) substrate.

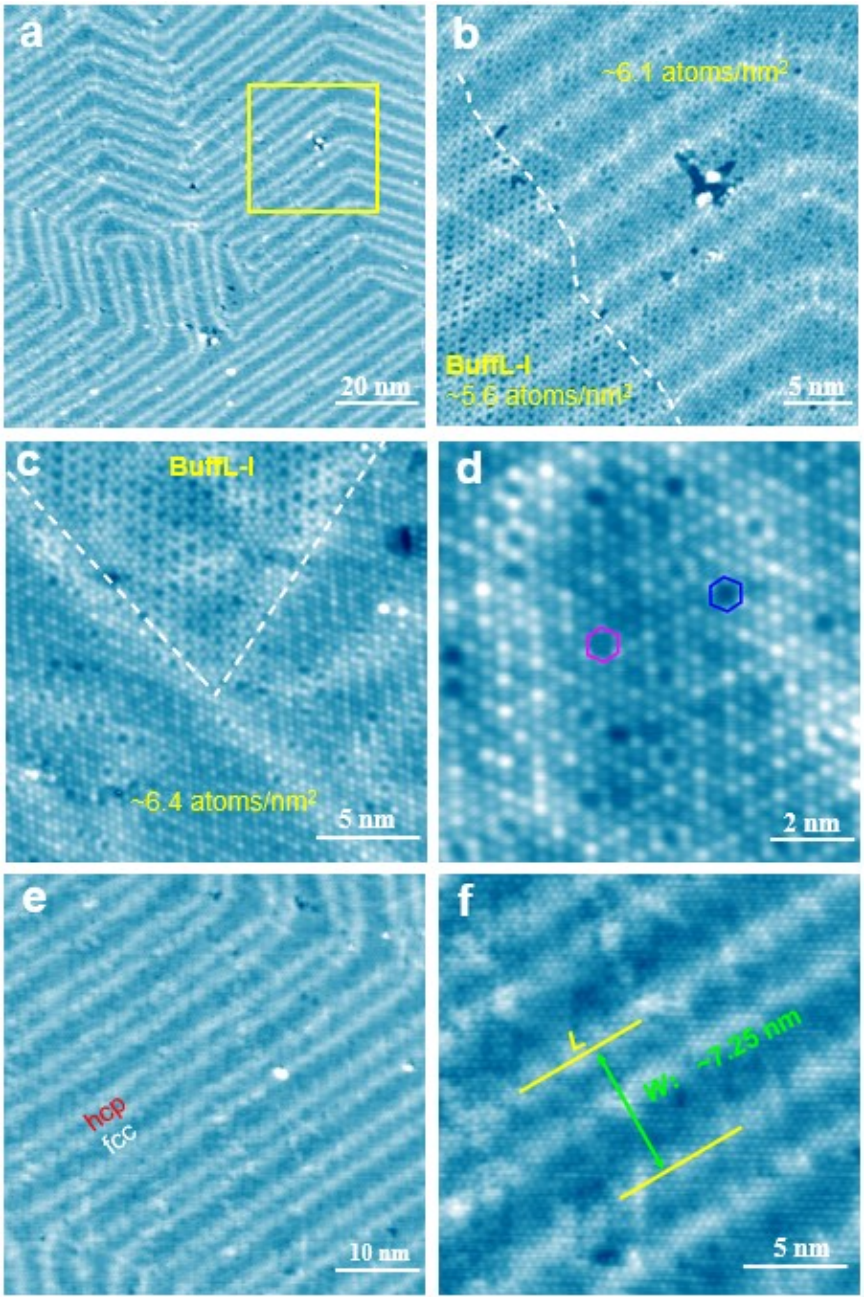

Figure S3. Other buffering layers. (a) A large-scale STM image of the mixture of Buff-I and a transitional phase. (b) Zooming in of the yellow square in panel (a), where the atomic density increases slightly in the transitional phase. (c-f) STM images of other close-packing configurations with less ordering and more defects. (a) V = 0.5 V, I = 100 pA; (b) V = -0.4 V, I = 400 pA); (c) V = 1 V, I = 200 pA; (d) V = 1 V, I = 500 pA; (e) V = -0.4 V, I = 400 pA; (f) V = -0.4 V, I = 400 pA.

BuffL-III layer is distinct from others due to its extraordinary herringbone structure and free of defect. The line profile presented in the inset of Figure S4a reveals a step height of 1.6 Å. From the large-scale images in Figure S4a-c, we can see that the surface is atomically smooth and uniform, with highly ordered herringbone-like stripes. The longest stripe observed in Figure S4a could reach over 300 nm without break. From Figure S4d, it is clear that the moiré-like superstructures are incommensurate with a wave-shape modulation.

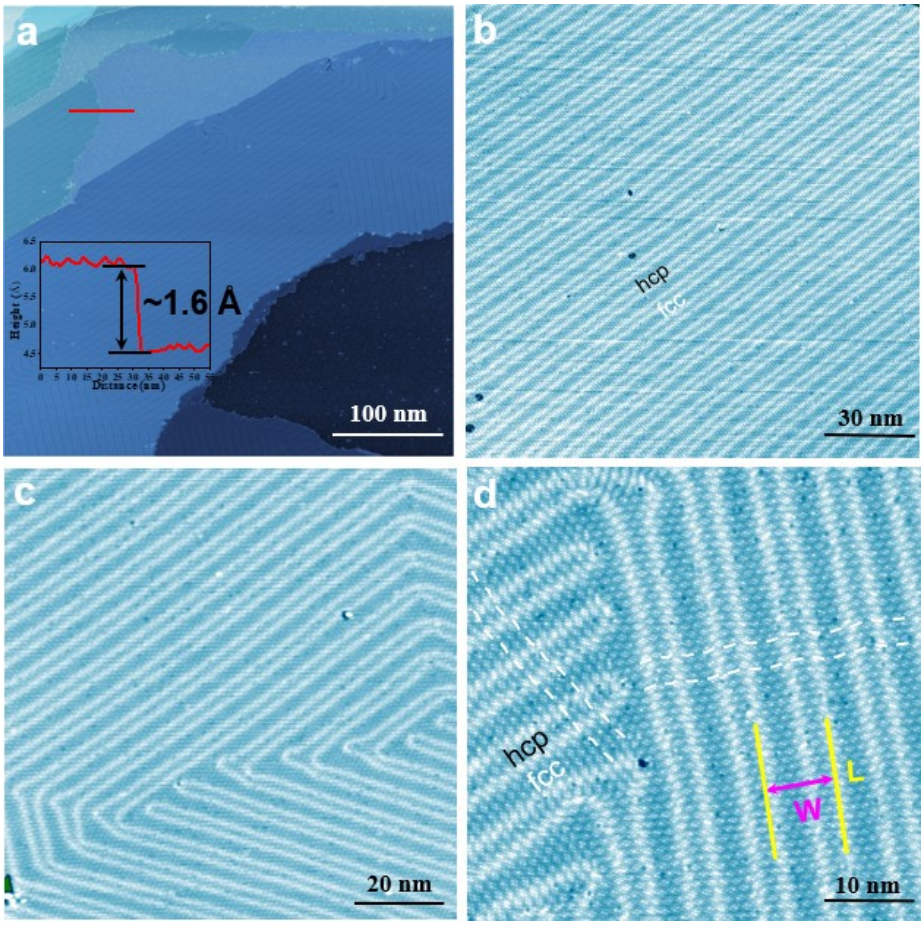

Figure S4. More STM images of the BuffL-III layer, revealing the highly ordered herringbone-like stripes. The inset in panel (a) shows the line profile corresponds to the red line. (a-d) $V = 0.4$ V, $I = 400$ pA.

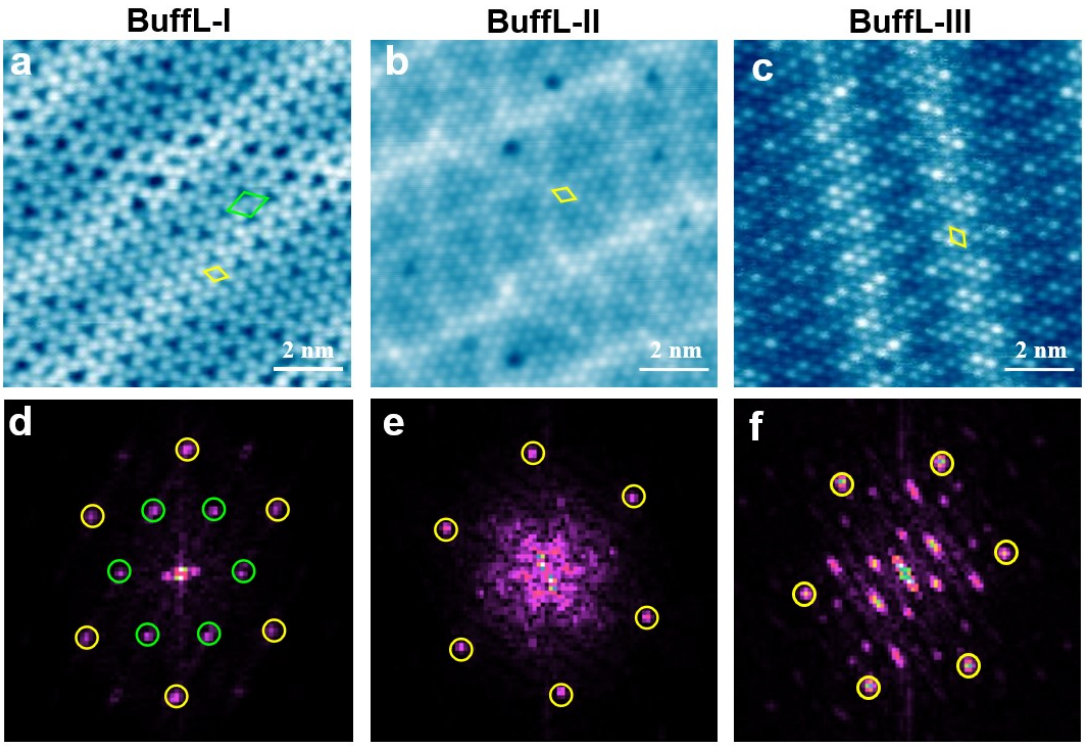

Figure S5. The complicated superstructures observed in the buffering layers. (a-c) Atomically resolved STM images and (d-f) their corresponding FFT patterns of BuffL-I, II and III, respectively. In each phase, the yellow circles correspond to the unit cell highlighted by the yellow rhombus. In BuffL-I, the superstructure attributes to the green circles are also highlighted.

Table S2. Summary of atomic density, lattice constant, intersection angle (with respect to Au(111)), and herringbone width (W) and length (L) of clean Au(111), $MnBr_x$ buffering layers, and $MnBr_2$ layers.

	Au(111)	**BuffL-I**	**BuffL-II**	**BuffL-III**	**Monolayer**	**Bilayer**
Density (atoms/nm^2)	11.8±0.2	5.6±0.1	6.5±0.2	6.6±0.2	6.8±0.1	6.8±0.1
Lattice constant (Å)	2.9±0.1	\	4.0±0.2	4.0±0.2	3.9±0.1	3.9±0.1
Intersection angle	0	50° ± 2°	69° ± 2°	29° ± 2°	62° ± 2°	62° ± 2°
Herringbone width (nm)	6.6±0.1	6.6±0.2	7.2±0.4	7.2±0.3	\	\
Herringbone length (nm)	5.3 - 40.1	>50	> 100	> 300	\	\

IV. $MnBr_2$ layers

Figure S6 shows high-resolution STM images recorded at the edge of $MnBr_2$ monolayers, where the coexistences of different buffering layers are observed in different areas. The $MnBr_2$ thin films only grow atop the $MnBr_x$ buffering layers but not Au(111) surface, which could reduce the strong hybridization between 2D materials and metal substrates. The inset of Figure S6b shows the line profile along the red line, revealing a step height of 3.6 Å. As indicated in Figure S6(a), the lattice orientation of $MnBr_2$ monolayer is of 62º±2º (β) with respect to Au(111),

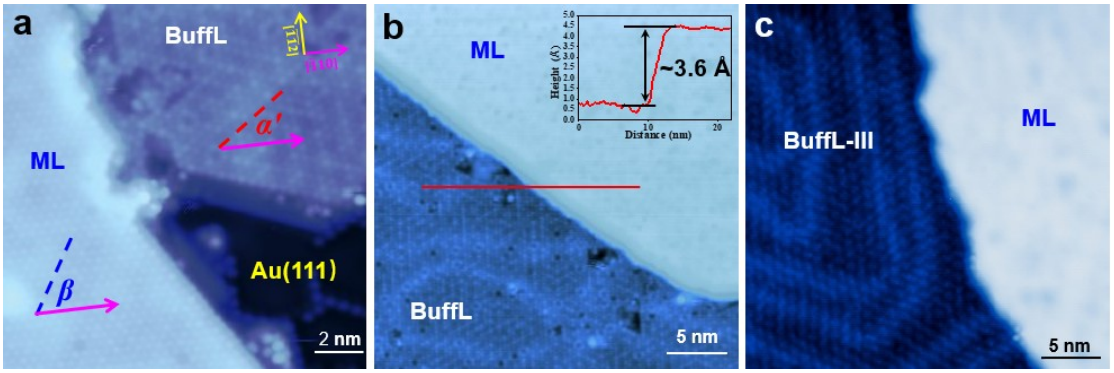

which are not the same as the buffering layering (α' = 35º±2º).

Figure S6. The growth of $MnBr_2$ monolayers atop buffering layers: (a) V = 0.2 V, I = 150 pA; (b) V = 1.0 V, I = 200 pA; (c) V = 1.0 V, I = 100 pA.

Figure S7a-e shows large-scale STM images of $MnBr_2$ thin films with increasing coverages. In Figure S7a, ~0.5 L $MnBr_2$ coexists with buffering layers, where the lateral profile corresponding to the red line is shown in Figure S7, combined with other line profiles demonstrated in insets, we confirm that the height of a single $MnBr_2$ layer is 3.3 – 3.6 Å, and a buffering layer is 1.3 – 1.6 Å determined by STM. The high-resolution STM image in Figure S7f shows the atomic structure of the ML with a few defects.

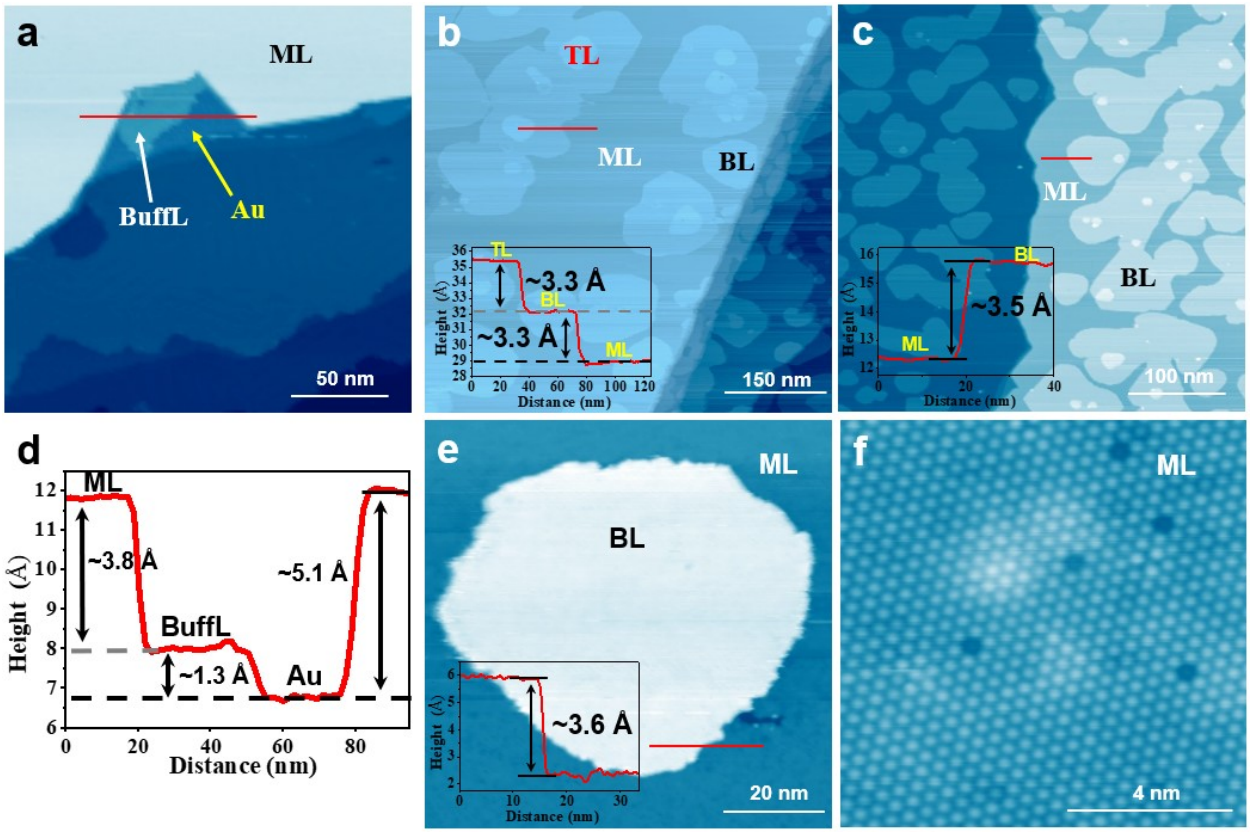

Figure S7. More images of $MnBr_2$ thin films. (a-c) Large-scale STM images with ML, BL, and TL layer regions. (d) The line profile corresponds to the red line in panel (a). (f) An atomically resolved image recorded at ML $MnBr_2$. (a) V = 1.0 V, I = 100 pA; (b) V = 1.0 V, I = 100 pA; (c) V = 1.0 V, I = 100 pA; (e) V = 1.0 V, I = 200 pA; (f) V = -1.8 V, I = 200 pA.

V. XPS measurements

Table S3. XPS fitting parameters for Mn $2p_{3/2}$, Au $4p_{1/2}$, satellites, Br $3d_{3/2}$, and Br $3d_{5/2}$ with binding energy (BE), full width at half maximum (FWHM), and area (A).

Sample	Peaks	BE (eV)	FWHM (eV)	Area
Au(111) with Br residual	Au $4p_{1/2}$	642.6	6.9	184275.55
	Br $3d_{5/2}$	67.6	0.85	2275.40
	Br $3d_{3/2}$	68.7	0.85	1355.37
0.6 L BuffL	Mn $2p_{3/2}$ 1	640.2	1.35	1535.49
	Mn $2p_{3/2}$ 2	641.2	1.35	7396.74
	Mn $2p_{3/2}$ 3	642.2	1.35	5128.73

	Mn $2p_{3/2}$ 4	643.2	1.35	3550.48
	Satellite	646.5	2.24	3355.41
	Br $3d_{5/2}$	68.6	0.94	6974.07
	Br $3d_{3/2}$	69.6	0.94	3401.18
	Au $4p_{1/2}$	642.6	6.9	119149.89
0.9 L BuffL	Mn $2p_{3/2}$ 1	640.2	1.36	1832.44
	Mn $2p_{3/2}$ 2	641.2	1.36	11039.20
	Mn $2p_{3/2}$ 3	642.2	1.36	8172.20
	Mn $2p_{3/2}$ 4	643.2	1.36	5439.58
	Satellite	646.5	2.24	5701.68
	Br $3d_{5/2}$	68.6	0.99	11651.27
	Br $3d_{3/2}$	69.6	0.99	6178.01
	Au $4p_{1/2}$	642.6	6.9	105080.62
1.1 L $MnBr_2$ on BuffL	Mn $2p_{3/2}$ 1	641.5	1.1	15898.56
	Mn $2p_{3/2}$ 2	642.6	1.1	10516.39
	Mn $2p_{3/2}$ 3	643.5	1.1	7897.30
	Mn $2p_{3/2}$ 4	644.5	1.1	3988.03
	Satellite	647.0	2.43	21101.23
	Mn $2p_{3/2}$ 1	640.2	1.35	1988.95
	Mn $2p_{3/2}$ 2	641.2	1.35	12303.55
	Mn $2p_{3/2}$ 3	642.2	1.35	8146.25
	Mn $2p_{3/2}$ 4	643.2	1.35	6235.07
	Satellite	646.5	2.24	5428.82
	Br $3d_{5/2}$	69.1	0.99	18115.22
	Br $3d_{3/2}$	70.1	0.99	12423.58
	Br $3d_{5/2}$	68.6	0.99	12131.31
	Br $3d_{3/2}$	69.6	0.99	6591.56
	Au $4p_{1/2}$	642.6	6.9	83669.02
2.1 L	Mn $2p_{3/2}$ 1	641.5	1.1	32298.29

$MnBr_2$ on BuffL	Mn $2p_{3/2}$ 2	642.6	1.1	19913.81
	Mn $2p_{3/2}$ 3	643.5	1.1	14922.35
	Mn $2p_{3/2}$ 4	644.5	1.1	5128.49
	Satellite	647.0	2.43	29230.21
	Mn $2p_{3/2}$ 1	640.2	1.35	1988.82
	Mn $2p_{3/2}$ 2	641.2	1.35	12302.91
	Mn $2p_{3/2}$ 3	642.2	1.35	7983.43
	Mn $2p_{3/2}$ 4	643.2	1.35	6234.88
	Satellite	646.5	2.24	9801.08
	Br $3d_{5/2}$	69.2	0.99	34323.98
	Br $3d_{3/2}$	70.2	0.99	24610.43
	Br $3d_{5/2}$	68.6	0.99	12131.04
	Br $3d_{3/2}$	69.6	0.99	6591.56
	Au $4p_{1/2}$	642.6	6.9	65460.9

As summarized in Table S4, we quantitatively analyze the intensities of Br $3d_{5/2}$ and Mn $2p_{3/2}$ (sum of the multiplets) peaks, which increase linearly with their coverages. The intensity for a single $MnBr_2$ layer (1 L) could be approximately estimated by A4-A3 or (A3-A2/0.9)/1.1, which are very close to each other. Furthermore, the ratio of A_{BuffL}:$A_{\text{1L-MnBr2}}$ could be obtained based on (A2/0.9)/(A4-A3), which is deduced to 0.72. This value is very close to 2:3. Considering that triple Br-Mn-Br structure for $MnBr_2$, the buffering layer might be composed of two atomic layers but nonstoichiometric structure.

Based on Avantage Data Analysis Manual provided by Thermo Fisher Scientific, $I_{normalised} = \frac{A}{S\sigma f}$,[6] where A is the peak area, S is the relative sensitivity factor, σ is the transmission function, and f is the energy compensation factor. The values of S, σ, and f are all provided by the Manual.

Table S4. Summary of the Br $3d_{5/2}$and Mn $2p_{3/2}$ peak areas of the samples shown in Figure 4, and the estimated stoichiometries.

Component	Area (Br $3d_{5/2}$)	Area (Mn $2p_{3/2}$)	*x* (Br:Mn)
2.1 L $MnBr_2$ on BuffL (A4)	46455.02	100772.98	1.66
1.1 L $MnBr_2$ on BuffL (A3)	30246.53	66974.1	1.83
0.9 L BuffL (A2)	11651.27	26483.42	1.98
0.6 L BuffL (A1)	6974.07	17611.44	1.99
1 L $MnBr_2$ (A4-A3)	16208.49	33798.88	/
1 L $MnBr_2$ [(A3-A2/0.9)/1.1]	15727.88586	34134.61616	/

In contrast, if we assumed that the buffering layers were converted (vanished) to $MnBr_2$ in the thick films. The intensity for a single $MnBr_2$ layer (1 L $MnBr_2$) could be approximately estimated by A4-A3 (16208.49) or A3/1.1 (27496.85) or A4/2.1 (22121.44), which are not consistent with each other. As thus, this possibility can be excluded.

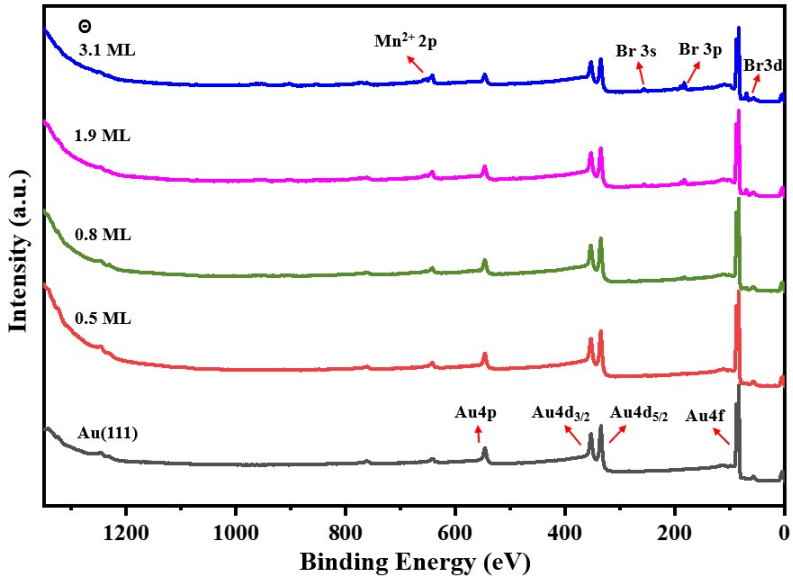

Figure S8. XPS full surveys of clean Au(111), buffering overlayers and $MnBr_2$ thin films. Each peak in the spectra is clearly assigned to the corresponding element. No extraneous peak is observed..

VI. DFT calculations

The work functions of isolated ML $MnBr_2$ and clean Au were calculated to elucidate the charge transfer behavior at the interface. As shown in Figure S9, their values are 4.93 eV and 5.52 eV for $MnBr_2$ and Au(111), respectively. Therefore, electrons transfer from $MnBr_2$ with lower WF to Au(111) with higher WF.

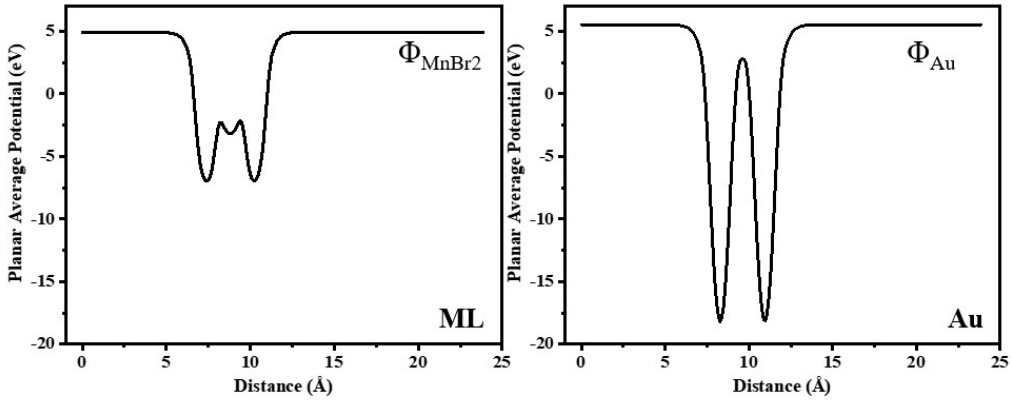

Figure S9. The calculated WF of ML $MnBr_2$ and clean Au.

To gain deeper insight into the spin-resolved electronic structure of $MnBr_2$, we calculated the band structure for the spin-up and spin-down channels separately. As shown in Figure S10, the intrinsic semiconducting bandgap of monolayer $MnBr_2$ remains clearly visible even in the presence of the Au(111) substrate. In the spin-up channel, the VBM is located at -1.30 eV, and the CBM appears at 0.60 eV, yielding a bandgap of 1.90 eV. Similarly, in the spin-down channel, the VBM and CBM are found at -1.50 eV and 0.40 eV, respectively, resulting in the same bandgap value of 1.90 eV.

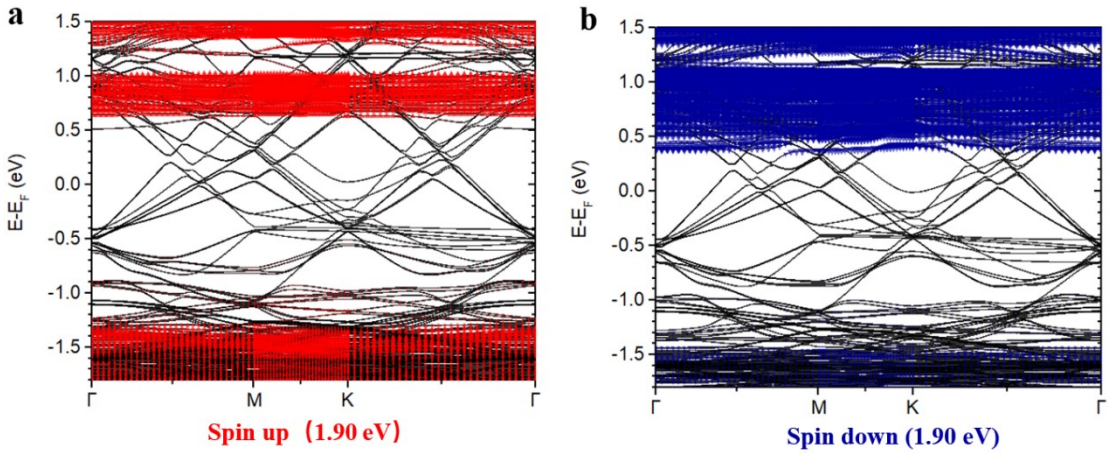

Figure S11. The spin-polarized band structures of the ML-$MnBr_2$/Au(111) system.

References

1 E. O. Wollan, W. C. Koehler and M. K. Wilkinson, *Phys. Rev.*, 1958, **110**, 638-646.
2 J. P. Perdew, K. Burke and M. Ernzerhof, *Phys. Rev. Lett.*, 1996, **77**, 3865-3868.
3 J. Heyd, G. E. Scuseria and M. Ernzerhof, *J. Chem. Phys.*, 2003, **118**, 8207-8215.
4 C. Woll, S. Chiang, R. J. Wilson and P. H. Lippel, *Phys. Rev. B: Condens. Matter*, 1989, **39**, 7988-7991.
5 J. V. Barth, H. Brune, G. Ertl and R. J. Behm, *Phys. Rev. B: Condens. Matter*, 1990, **42**, 9307-9318.
6 Thermo Fisher Scientific, Avantage Data Analysis Manual, Version 6, Thermo Fisher Scientific, Waltham, MA, 2023.